EES Batteries

PAPER

View Article Online
View Journal

Cite this: DOI: 10.1039/d6eb00089d

Interfacial strain engineering induces fatigue-resistant, high-capacity photo-assisted lithium storage

Mudasar Nazir,[a] Kiem G. Nguyen,[a] Richard T. Baker,[b] Matthew E. Berry,[c] Rabia Khatoon,[a] Shumaila Babar,[a] Steven Dunn,[a] Suela Kellici *[a] and Muhammad Tariq Sajjad *[a]

Mechanical fatigue, rather than redox instability, often limits the lifetime of high-capacity battery electrodes, as repeated ion insertion induces microstrain, cracking, and interfacial failure. Here, we show that interfacial strain engineering can be used to mitigate this vulnerability, enabling improved cyclability and capacity in metal-ion systems. Using a multiphase $TiO_2/K_2Ti_4O_9$-reduced graphene oxide composite as a model platform, we demonstrate that interfacial strain arising from intimately coupled oxide–oxide and oxide–carbon interfaces enhances photo-assisted lithium storage and contributes to fatigue-resistant cycling behaviour. These strain-modulated interfaces promote charge separation, improve Li^+ transport, and help to stabilise the electrode framework against repeated volume fluctuations. The photoelectrode delivers a light-enhanced capacity of ~534 mAh g^{-1} at 0.1C, exceeding the theoretical limit of TiO_2, and retains >86% of its capacity after 300 cycles at 1C. Operando Raman microscopy, together with *ex situ* and post-mortem analyses, shows that strain relaxation correlates with suppressed disorder accumulation and delayed interfacial degradation. These findings highlight interfacial strain engineering as a promising strategy for stabilising high-capacity electrodes in photo-assisted and broader battery chemistries limited by mechanically driven capacity fade.

Received 23rd April 2026,
Accepted 24th April 2026

DOI: 10.1039/d6eb00089d

rsc.li/EESBatteries

Broader context

Achieving durable, high-energy-density batteries is essential for electrified transport, renewable energy integration, and grid-scale storage. However, electrode lifetime is increasingly limited by mechanical degradation rather than electrochemical instability. Repeated volume changes during cycling lead to lattice fatigue, interfacial failure, and uncontrolled solid–electrolyte interphase growth, reducing efficiency and increasing material waste. This work demonstrates that interfacial strain engineering can transform strain from a driver of failure into a stabilising mechanism, enabling reversible lattice deformation and suppressing mechanically driven degradation. By identifying strain-induced fatigue resistance as a transferable design principle, the study offers a general strategy for improving durability across lithium-, sodium-, and conversion-type batteries, including high-capacity systems such as lithium–sulfur. Mechanically informed materials design is therefore critical for developing longer-lasting, resource-efficient energy-storage technologies with reduced environmental and economic cost.

1. Introduction

Mechanical degradation arising from repeated volume changes remains one of the most fundamental barriers to achieving durable, high-capacity battery electrodes. Across lithium-, sodium-, and conversion-type battery chemistries, lattice fatigue, crack formation, and interfacial failure, rather than intrinsic redox instability, often dictate practical lifetime and capacity retention.[1–7] Extensive studies on alloying and conversion electrodes have shown that cyclic stress accumulation driven by large volume fluctuations leads to particle fracture, loss of electrical contact, and rapid capacity fade.[5,6] While electrolyte and interface optimisation can mitigate some degradation pathways, mechanically driven failure remains a pervasive and largely unresolved limitation in next-generation energy-storage systems.[1]

While strain engineering has traditionally been explored as an approach to tune electronic structure or enhance charge transport, its role in suppressing mechanically driven degradation remains underdeveloped. Engineered strain fields offer the potential to redistribute stress, stabilise repeated ion inser-

[a]School of Engineering and Design, London South Bank University, 103 Borough Road, London, SE1 0AA UK. E-mail: kellicis@lsbu.ac.uk, sajjadt@lsbu.ac.uk
[b]EaStChem School of Chemistry, University of St Andrews, St Andrews KY16 9ST, UK
[c]Edinburgh Instruments Ltd, Livingston EH54 7DQ, UK

tion and extraction, and delay the onset of lattice fatigue.[8–10] However, conventional strain-engineering approaches, such as epitaxial mismatch, external mechanical bias, or ion implantation, often suffer from limited scalability, poor long-term stability, or the introduction of irreversible defects.[9] Developing intrinsically strain-buffered electrode architectures therefore represents an opportunity to address failure modes common to high-capacity battery materials.

Photo-assisted lithium-ion batteries provide a useful platform for interrogating these mechanically driven degradation processes, as they combine deep electrochemical cycling with additional carrier injection that amplifies interfacial stress and lattice response.[11–13] In oxide-based photoelectrodes, repeated ion insertion and extraction commonly induces microstrain, defect generation, and interfacial disorder during prolonged cycling, limiting practical durability even when electrochemical kinetics are favourable.[11,12] As such, photo-assisted systems offer a sensitive model framework for probing the interplay between strain evolution, lattice stability, and long-term performance across energy-storage materials.

Here, we demonstrate that interfacial strain engineering can be used to mitigate lattice-fatigue-related degradation in high-capacity battery electrodes. Using a scalable continuous hydrothermal flow synthesis route, we construct a multiphase $TiO_2/K_2Ti_4O_9$-reduced graphene oxide composite in which intimately coupled oxide–oxide and oxide–carbon interfaces generate interfacial strain. The resulting strain-perturbed hierarchical architecture enables enhanced photo-assisted lithium storage, with capacities of ~534 mAh g^{-1} at 0.1C, exceeding the theoretical limit of anatase TiO_2 (335 mAh g^{-1}). Operando Raman microscopy, supported by *ex situ* and post-mortem characterisation, indicates that strain relaxation is associated with suppressed disorder accumulation and delayed interfacial degradation during extended cycling. Importantly, this stabilisation mechanism is not specific to photo-assisted lithium storage and is directly relevant to battery chemistries dominated by mechanically driven failure, including lithium–sulfur and sodium-ion systems.[4,14] Interfacial strain engineering therefore emerges as a general design principle for durable, high-capacity energy-storage materials.

2. Experimental section

2.1 Synthesis of $TiO_2/K_2Ti_4O_9$-rGO nanocomposites

$TiO_2/K_2Ti_4O_9$-reduced graphene oxide (rGO) nanocomposites were synthesised using a continuous hydrothermal flow synthesis (CHFS) system,[15] as schematically illustrated in Scheme 1. Titanium(IV) bis(ammonium lactato) dihydroxide (Sigma-Aldrich, UK) was used as the titanium precursor (0.2 M). A potassium hydroxide (KOH, ≥85%, Sigma-Aldrich, UK)/graphene oxide (LayeredOne, Netherlands) feed solution was prepared by dispersing graphene oxide (GO, 0.5 mg mL^{-1}) in KOH (0.1 M) under sonication to ensure homogeneous dispersion. A reference TiO_2 sample was also synthesised under identical CHFS conditions in the absence of KOH and GO.

The CHFS system comprised three high-pressure pumps operating at 24.8 MPa. Deionised water (18.2 MΩ) was delivered to a tubular heater by Pump 1 at a flow rate of 20 mL min^{-1} and heated to supercritical conditions (450 °C). The titanium precursor solution and the KOH–GO mixture were introduced *via* Pumps 2 and 3, respectively, each at a flow rate of 10 mL min^{-1}. Rapid mixing under supercritical conditions induced instantaneous nucleation and non-equilibrium crystallisation, yielding a multiphase oxide–titanate composite with built-in interfacial strain. The product suspension was subsequently cooled *via* a heat exchanger and collected at the outlet of the back-pressure regulator (BPR).

The resulting suspension was collected, centrifuged (10 127*g* for 15 mins), and washed three times with deionised water to remove residual ions. The recovered solids were freeze-dried (–50 °C for 24 h) to obtain fine powders, denoted as $TiO_2/K_2Ti_4O_9$-rGO.

Materials characterisation. The morphology and microstructure of the synthesised powders and electrodes were examined using scanning electron microscopy (SEM; Zeiss Supra 55 VP)

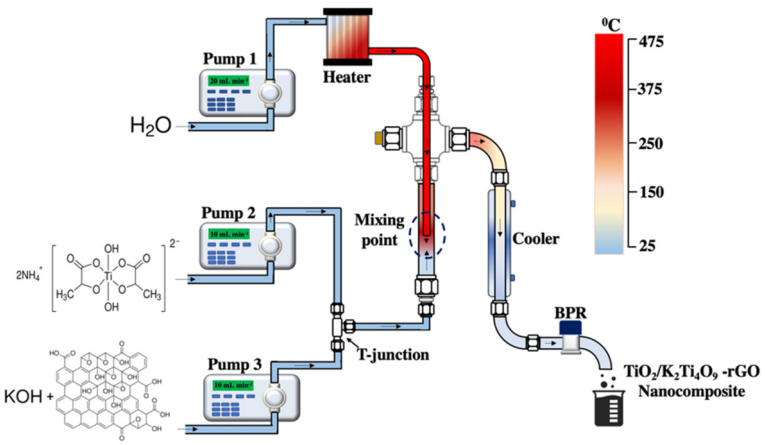

Scheme 1 Continuous hydrothermal flow synthesis of $TiO_2/K_2Ti_4O_9$-rGO.

operated at 10 kV. Phase composition and crystallinity were analysed by X-ray diffraction (XRD) using a Bruker D8 Advance diffractometer with Cu Kα radiation (λ = 1.5406 Å).

TEM images were obtained in both Transmission Electron Microscope (TEM) and Scanning TEM modes using a Titan Themis 200 keV (FEI) Transmission and Scanning Transmission Electron Microscope (S/TEM) equipped with an X-FEG Schottky field emission gun, CEOS DCOR spherical aberration corrector, and an ultra-stable 5 axis piezo-stage with drift compensation. Its Super-X high sensitivity windowless X-ray Energy Dispersive Spectroscopy (EDS) detector was used to perform area analyses and generate two-dimensional maps of the elemental composition of the samples. Digital Diffraction S/TEM images were analysed using DigitalMicrograph and ImageJ software. For study in the S/TEM, samples were crushed, suspended in acetone by ultrasonication and deposited onto holey carbon-coated Cu grids.

XPS measurements were performed in an ultrahigh vacuum chamber (~1×10^{-10} mbar) using a Kratos Axis Ultra DLD photoelectron spectrometer equipped with a monochromatic Al Kα (1486.6 eV) anode, operating at 4 mA and 15 kV. Wide scans were recorded, and high-resolution scans were obtained for selected individual elements for each sample. All binding energies were charge-corrected to the C 1s signal at 284.8 eV. Peak fitting was performed using CasaXPS software, version 2.3.25, with internally consistent assignments for Ti 2p, O 1s, K 2p, and C 1s components.

Raman spectra were acquired using an RMS1000 confocal Raman microscope (Edinburgh Instruments) equipped with 532 nm and 785 nm lasers; all spectra discussed herein were collected using the 532 nm excitation source over the range 100–1600 cm^{-1}. Fourier-transform infrared (FTIR) spectroscopy (IR Affinity-1S) was employed to probe chemical bonding and functional groups in the range 500–4000 cm^{-1}. Diffuse-reflectance UV–visible spectra were recorded using a Shimadzu UV-1800 spectrophotometer to estimate optical bandgaps. Ultraviolet photoelectron spectroscopy (UPS) measurements were conducted using a Thermo NEXSA system with He I radiation (21.2 eV) and an applied bias of −9 V.

Thermogravimetric analysis (TGA; Mettler Toledo DSC/TGA 3+) was performed from 25 to 1100 °C at a heating rate of 10 °C min^{-1} under air flow to determine rGO content and thermal stability. Specific surface areas were measured using nitrogen adsorption (Micromeritics Gemini VII) based on the Brunauer–Emmett–Teller (BET) method; samples were degassed at 180 °C for 2 h prior to analysis.

Electrode fabrication and electrochemical measurements. Working electrodes were prepared by mixing 80 wt% TiO_2/$K_2Ti_4O_9$-rGO active material, 10 wt% Super P conductive carbon, and 10 wt% polyvinylidene fluoride (PVDF) binder in *N*-methyl-2-pyrrolidone (NMP) to form a homogeneous slurry. The slurry was doctor-blade coated onto carbon felt substrates and dried under vacuum at 70 °C overnight. Circular electrodes (16 mm diameter) were punched from the dried films. Specific capacities were calculated with respect to the mass of the TiO_2/$K_2Ti_4O_9$-rGO active material.

Electrochemical cells were assembled in an argon-filled glovebox (O_2 and H_2O < 1 ppm) using lithium metal foil as the counter electrode and a Celgard 2500 polypropylene membrane as the separator. The electrolyte consisted of 1.0 M $LiPF_6$ dissolved in a 1 : 1 (v/v) mixture of ethylene carbonate (EC) and diethyl carbonate (DEC). A photocell configuration incorporating a quartz window was employed to enable *in situ* illumination during testing.

Electrochemical measurements, including cyclic voltammetry (CV), galvanostatic charge–discharge (GCD), and electrochemical impedance spectroscopy (EIS), were conducted using a Biologic SP-300 potentiostat. Illumination was provided by an Oriel Sol1A solar simulator operating under AM 1.5 G conditions. EIS measurements were recorded over a frequency range of 10 mHz to 100 kHz under both dark and illuminated conditions with a 10 mA perturbation current.

Operando Raman spectroscopy. Operando Raman spectroscopy was performed using a 532 nm Nd:YAG laser (5 mW incident power) coupled to the RMS1000 confocal Raman microscope. Spectra were collected using a 1200 g mm^{-1} grating and a thermoelectrically cooled CCD detector. During electrochemical cycling, Raman spectra were acquired in kinetic mode with 12 accumulations and an acquisition time of 60 s per spectrum, enabling real-time tracking of strain evolution, disorder accumulation, and interfacial degradation over extended cycling.

Confocal Raman microscopy. Fresh and cycled electrodes were analysed by two-dimensional confocal Raman mapping. The acquired Raman imaging data were processed using Ramacle® in a Python IDE, where cosmic ray removal was applied prior to analysis. Chemometric analysis was subsequently performed using non-negative least squares (NNLS) unmixing to resolve the spatial distribution of the constituent components.

3. Results and discussion

3.1 Synthesis and characterisation of strain-engineered multiphase architecture

The strain-engineered multiphase architecture was produced *via* a single-step, ultrafast continuous hydrothermal flow synthesis strategy. Rapid supersaturation and non-equilibrium crystallisation pathways produce structurally complex multiphase systems. The CHFS approach enables precise control over phase formation and lattice distortion. This generates a strongly integrated multiphase heterostructure composed of anatase TiO_2, metastable TiO_2(B), and layered $K_2Ti_4O_9$ integrated within a reduced graphene oxide (rGO) framework. TiO_2(B) is challenging to stabilise under conventional conditions. CHFS enabled by rapid supersaturation and the presence of KOH and GO drives its formation through a sequential titanate-to-titania transformation. This drives controlled distortion within anatase and $K_2Ti_4O_9$ lattices. The resulting architecture integrates multiple lithium-hosting domains with tailored interfacial chemistry. This underpins enhanced photoelectrochemical performance.

High-resolution TEM reveals a multiphase architecture comprising anatase nanoparticles (3–11 nm), TiO_2(B) nanorods, and layered $K_2Ti_4O_9$ platelets intimately integrated within a reduced graphene oxide (rGO) scaffold (Fig. 1a–c and Fig. S1, S2). These closely coupled phases create numerous oxide–oxide and oxide–carbon junctions. At several boundaries, lattice bending, fringe curvature, and local discontinuities are observed (Fig. 1a and S1), which are consistent with local lattice distortion and interfacial strain generated during rapid, non-equilibrium crystallisation under CHFS conditions. Measured interplanar spacings of ~0.88 nm and ~0.63 nm correspond to layered $K_2Ti_4O_9$ and TiO_2(B)/(anatase) domains, respectively, confirming coexistence of all target phases (Fig. S1a).[16,17]

The lattice fringes in the particles indicated in Fig. 1a and S1 exhibit pronounced distortion near particle boundaries, consistent with strain gradients developing from particle interiors toward the surface, indicative of strain-modulated crystal growth.[18] Importantly, these distortions occur without evidence of cracking or amorphisation, suggesting that strain is elastically accommodated across multiphase junctions rather than leading to structural failure. This multiphase framework yields a high BET surface area of 159 $m^2\ g^{-1}$ and an interconnected network favourable for Li^+ transport. Rather than functioning solely as a high-surface-area morphology, the architecture behaves as a mechanically compliant network, in which strain is redistributed across oxide–oxide interfaces and buffered by the rGO scaffold. This enables reversible lattice deformation during repeated Li^+ insertion and extraction, suppressing stress localisation and underpinning the fatigue-resistant electrochemical behaviour observed during prolonged cycling (section 2.2–2.5).

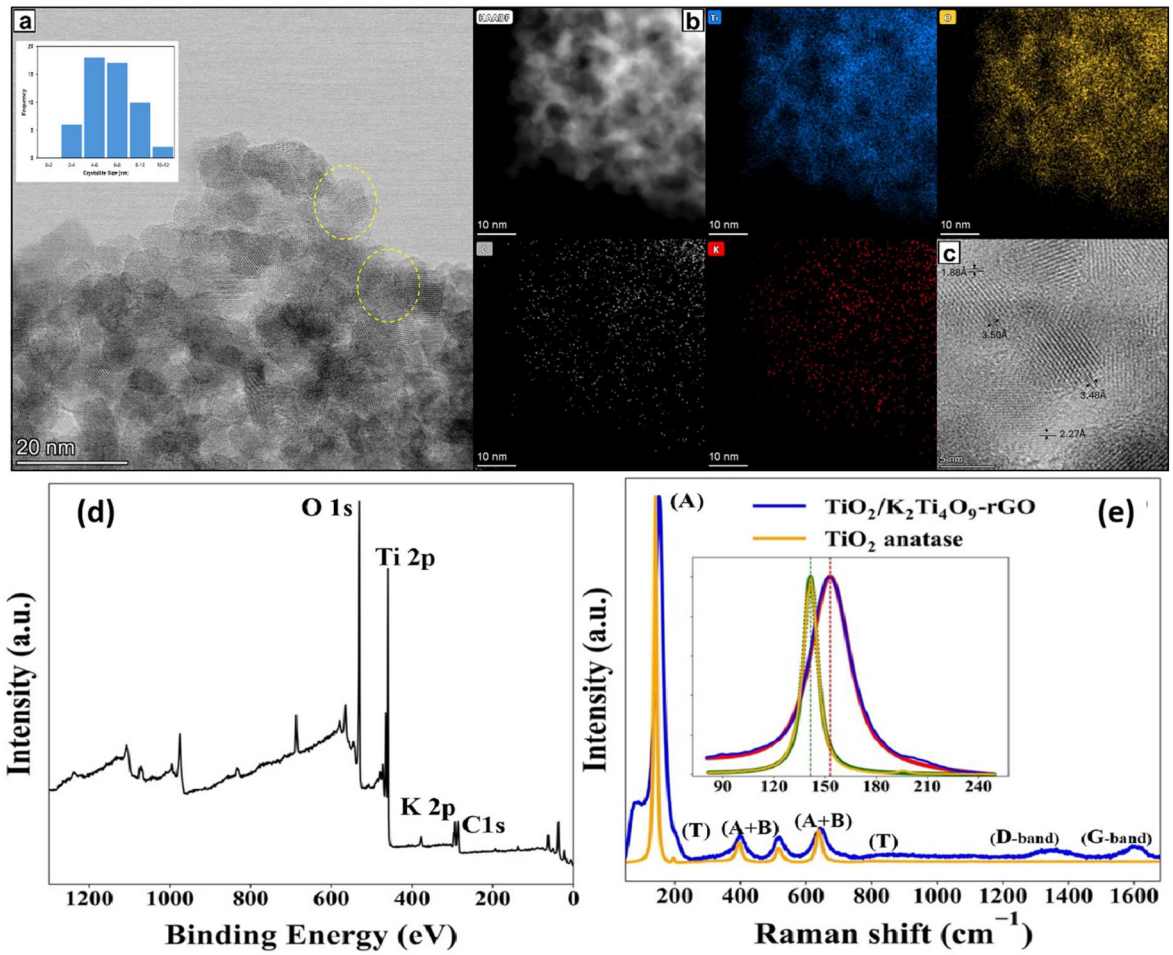

Fig. 1 Strain-engineered multiphase $TiO_2/K_2Ti_4O_9$-rGO architecture. (a) Intermediate magnification Bright-field TEM image showing clusters of nanoparticles; inset shows particle size distribution (n > 50 particles, mean 6.5 nm). Defective regions with non-linear lattice planes are circled. (b) High Angle Angular Dark Field (HAADF)image with corresponding EDS elemental maps, confirming uniform spatial distribution of Ti, O, K, and intimate integration of the C-containing phase. (c) High-magnification Bright Field TEM image showing the lattice fringes corresponding to anatase and TiO_2(B) crystallites. The spacings at 1.88 Å are consistent with the (020) planes of the anatase structure, while those at 3.48/3.50 Å are closest to anatase (011) and those at 2.27 Å are closest to TiO_2(B) ($\bar{3}12$). (d) XPS survey spectrum confirming the presence of Ti, O, K, and C. (e) Raman spectra showing characteristic modes of anatase (A), TiO_2(B), and $K_2Ti_4O_9$ (T), along with D/G bands of rGO. The pronounced blue shift and broadening of the anatase E_g mode indicate compressive strain within the heterostructure.

XPS and Raman spectroscopy (Fig. 1d and e) provide complementary evidence for a mixed-valence, defect-rich interfacial environment in the multiphase architecture. Raman analysis (inset, Fig. 1e) shows a blue shift of the anatase E_g mode from 146.6 to 153.1 cm^{-1} and peak broadening from 15 to 25 cm^{-1}, consistent with compressive lattice perturbation and local disorder. The estimated Raman-derived strain (~1.5%; see SI) is treated here as an approximate effective value, since phonon confinement, finite crystallite size, and surface/disorder effects may also contribute. XPS further reveals Ti^{4+}/Ti^{3+} coexistence and modified oxygen environments, supporting the presence of defect-rich interfaces. Together, these spectroscopic results support a strain-perturbed lattice/electronic landscape that likely contributes to the improved electrochemical and photoelectrochemical performance.

UV–Vis and UPS measurements (Fig. S4, S5, and S6) were used to evaluate the energetic feasibility of the interfacial charge-transfer pathway. The combined data suggest a favourable band alignment among anatase, TiO_2(B), and $K_2Ti_4O_9$, consistent with a cascade-type electronic structure that facilitates stepwise electron transfer across the multiphase interfaces (Fig. S6). The conduction bands of anatase and TiO_2(B) lie slightly above that of $K_2Ti_4O_9$, making electron transfer to $K_2Ti_4O_9$ energetically favourable. rGO, with a lower-lying electronic level, acts as an electron-accepting pathway that aids carrier extraction and suppresses recombination. This band configuration supports the energetic plausibility of improved carrier separation and transport, in agreement with the enhanced photo-assisted charging behaviour observed in the composite.

The CHFS-derived architecture integrates (i) strain-engineered, defect-rich interfaces, (ii) mechanically compliant multiphase domains, and (iii) percolating electron pathways through rGO. This hierarchical, strain-modulated structure offers a high density of active interfacial sites. Superior electrochemical kinetics and long-term stability are promoted through accelerated Li^+ diffusion pathways and a resilient framework that mitigates structural fatigue.

3.2. Electrochemical performance in the dark

The electrochemical measurements under dark conditions demonstrate that interfacial strain plays a central role in stabilising repeated volume fluctuations and suppressing crack formation during prolonged cycling. The strain-engineered TiO_2/$K_2Ti_4O_9$-rGO composite displays improved electrochemical behaviour compared to pure TiO_2 or $TiO_2/K_2Ti_4O_9$ (Fig. 2a and S8). Cyclic voltammetry (CV) shows sharper, more intense redox peaks (Fig. 2b). This demonstrates accelerated kinetics and efficient multiphase lithiation. At 0.1C, galvanostatic cycling delivers ~325 mAh g^{-1}(Fig. 2c). This approaches the theoretical capacity of TiO_2 (335 mAh g^{-1}) and exceeds conventional TiO_2-based electrodes. Kinetic limitations are more restrictive at a cycling rate of 1C. However, the composite electrode maintains ~225 mAh g^{-1}after 100 cycles and ~175 mAh g^{-1} after 300 cycles. This outperforms both pure TiO_2 and $TiO_2/K_2Ti_4O_9$ electrodes (Fig. 2d). The high-rate capacity reten-

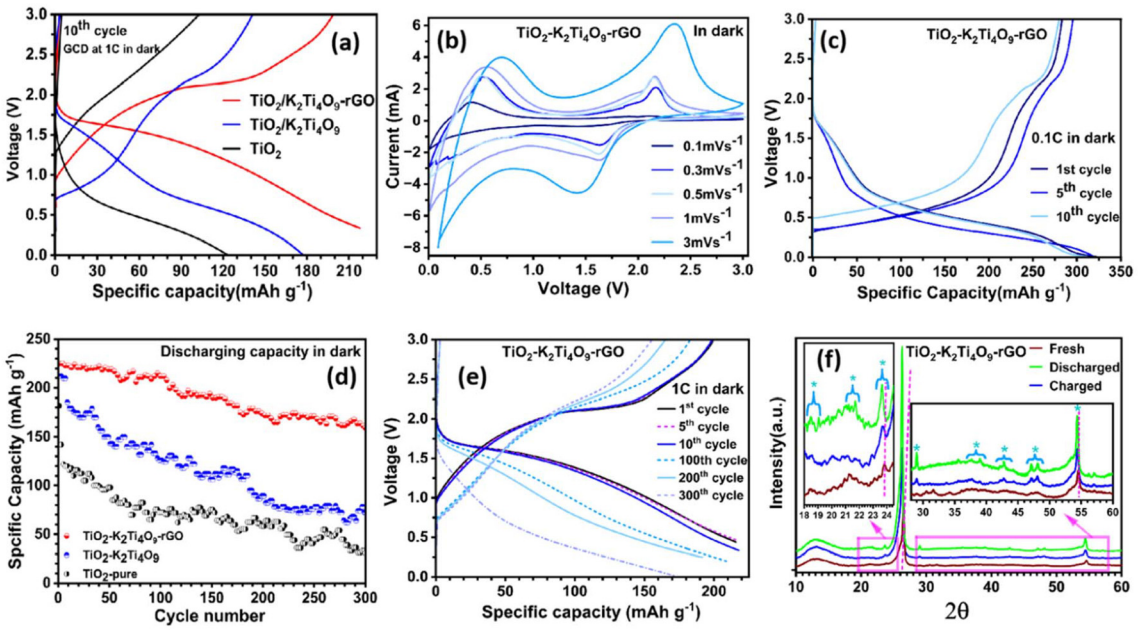

Fig. 2 Fatigue-resistant electrochemical behaviour under dark conditions. (a) Galvanostatic charge/discharge profiles of pure TiO_2, $TiO_2/K_2Ti_4O_9$, and $TiO_2/K_2Ti_4O_9$-rGO electrodes. (b) Cyclic voltammograms recorded at 0.1–3 mV s^{-1}, showing well-defined redox peaks associated with multiphase lithiation/delithiation. (c) Galvanostatic cycling at 0.1C, demonstrating a high reversible capacity (~325 mAh g^{-1}). (d) Long-term cycling stability of pure TiO_2, $TiO_2/K_2Ti_4O_9$, and $TiO_2/K_2Ti_4O_9$-rGO electrodes over 300 cycles. (e) Cycling at 1C, highlighting sustained capacity retention. (f) *Ex situ* XRD patterns of pristine, charged, and discharged electrodes after 300 cycles at 1C, showing reversible lattice expansion/contraction and strain-accommodated structural evolution without phase collapse.

tion (~78%) underscores the mechanical robustness of the strain-engineered framework. It further highlights the role of interfacial strain in stabilising repeated volume fluctuations and suppressing crack formation.

Ex situ XRD (Fig. 2f) reveals small but fully reversible 2θ shifts during charge/discharge. This is consistent with strain-accommodated lattice breathing rather than irreversible phase transformation. Peak broadening remains modest; no new phases are detected. Characteristic reflections of anatase, TiO_2(B), and $K_2Ti_4O_9$ are preserved throughout cycling, indicating retention of the multiphase framework. An additional XRD peak associated with the intermediate Li_x[TiO_2/$K_2Ti_4O_9$rGO] emerges during discharge at ~23.85°. This is consistent with deep Li^+ insertion enabled by the compliant architecture. These observations show that the hierarchical composite behaves as a strain-buffered Li host, capable of sustaining repeated cycling without obvious phase collapse. Compared with phase-pure TiO_2, which rapidly loses capacity, the multiphase composite exhibits greater structural resilience, likely because of engineered strain fields, closely coupled multiphase interfaces, and rGO-mediated electronic conductivity.

3.3. Photo-assisted lithium storage

Illumination enhances the electrochemical response of the strain-engineered TiO_2/$K_2Ti_4O_9$-rGO composite. Under AM 1.5 G illumination, the CV currents more than double and redox overpotentials decrease significantly (Fig. 3a and b). This indicates that photogenerated carriers accelerate interfacial charge transfer. Illumination therefore enhances charge-transfer kinetics while simultaneously promoting strain relaxation that suppresses fatigue-driven degradation during repeated cycling. The CV profiles maintain symmetric anodic and cathodic peaks, confirming highly reversible photo-assisted kinetics. The integrated CV area, proportional to stored charge, nearly triples (Fig. 3a and b). These features demonstrate that injected electrons actively participate in the redox process and lower the activation barrier for Li^+ insertion.

Under illumination, the electrode reaches ~534 mAh g^{-1} at 0.1C, a 64% enhancement over the dark value (~325 mAh g^{-1}) (Fig. 3d). This value exceeds the theoretical capacity of single-phase anatase TiO_2 (335 mAh g^{-1}). This higher capacity is attributed to the combined contribution of TiO_2(B) and $K_2Ti_4O_9$ lithium-storage pathways, interfacial/defect-assisted storage, and improved utilization under illumination. At 1C (Fig. 3c and d), where diffusion limitations dominate, illumination boosts capacity from ~225 to ~325 mAh g^{-1} after 100 cycles and maintains ~285 mAh g^{-1} up to 300 cycles, highlighting the beneficial interaction between multiphase interfaces and photoexcited carrier dynamics.

This higher capacity arises from two mechanisms: (i) photocarrier-assisted lithiation, where injected electrons enrich Ti^{3+} states and accelerate charge transfer; and (ii) strain-activated

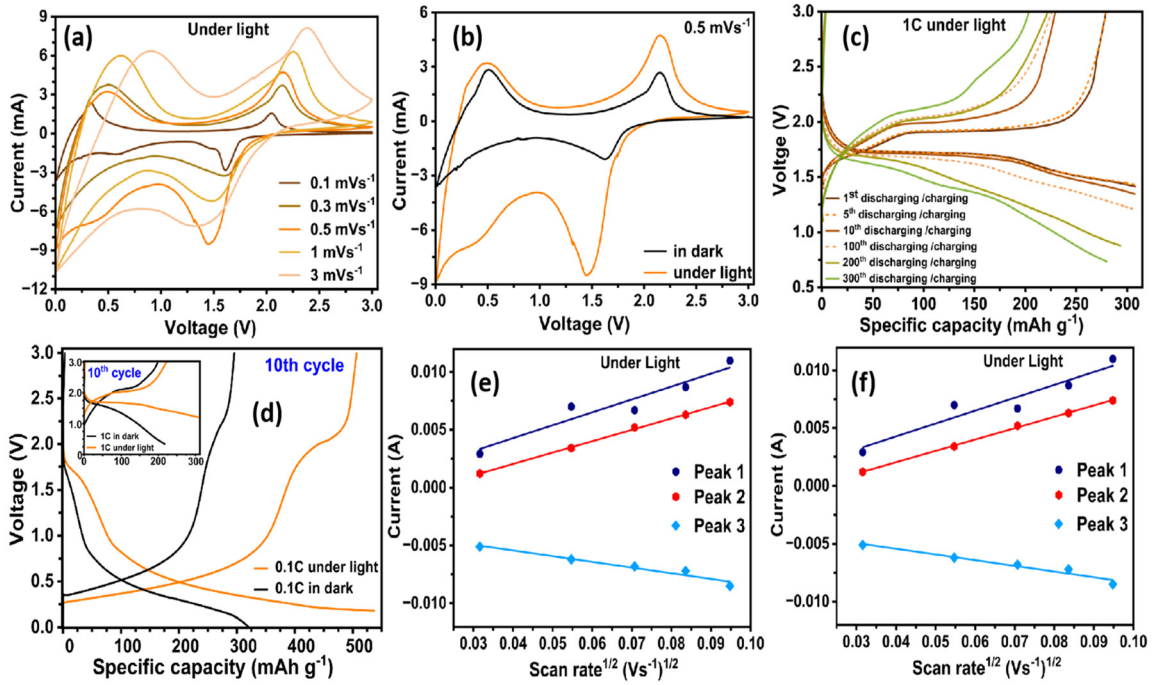

Fig. 3 Photo-assisted lithium storage and interfacial kinetics. (a) CV curves recorded at different scan rates under illumination, showing increased current density and reduced overpotentials. (b) Comparison of CV curves recorded at 0.5 mV s^{-1} in the dark and under illumination, highlighting the expanded charge-storage area under light. (c) Galvanostatic charge–discharge (GCD) profiles at 1C under illumination, showing the 1st, 5th, 10th, 100th, 200th, and 300th cycles. (d) Comparison of 10th cycle GCD curves at 0.1C and 1C (inset) in light and dark, demonstrating >40% photo-enhancement. (e and f) Randles–Sevcik analysis showing linear dependence of peak current on square root of the scan rate ($v^{1/2}$) and a two-order-of-magnitude increase in the apparent Li^+ diffusion coefficient under illumination.

diffusion channels, in which illumination induces local lattice expansion that unlocks previously inaccessible Li^+ insertion sites. Randles–Sevcik analysis confirms this behaviour[14,19] (Fig. 3e, f, and S10). The apparent Li^+ diffusion coefficient increases from 7.9×10^{-10} cm^2 s^{-1} (dark) to 3.7×10^{-8} cm^2 s^{-1} (illuminated), a two-order-of-magnitude enhancement (Table S2). This increase shows that photocarriers do not simply add charge, they also activate strain-modulated transport channels, reduce interfacial barriers, and promote deeper lithiation.

Rate-dependent cycling behaviour further highlights the effect of illumination. Across 0.1–2C (Fig. 4a), all electrodes exhibit an initial equilibration phase followed by rapid capacity stabilisation. This demonstrates the robustness of the strain-engineered multiphase framework. At 0.1C, the capacities at the 5th and 40th cycles are almost indistinguishable in both dark and light conditions. This is due to the efficient ion transport supported by the $TiO_2/K_2Ti_4O_9$-rGO architecture and the conductive rGO scaffold.

Long-term cycling at 1C further highlights the stabilising influence of illumination (Fig. 4b). Under AM 1.5 G illumination, the electrode retains >280 mAh g^{-1} after 300 cycles with ~100% coulombic efficiency, whereas the dark-cycled analogue decays to ~190 mAh g^{-1} with an efficiency of ~93%. This demonstrates that photocarriers not only enhance charge-transfer kinetics but also stabilise the electrode architecture and suppress long-term degradation. Illumination also enables capacity regeneration in severely fatigued electrodes. After extensive cycling in the dark (up to 600 cycles), a 3-hour rest under light restores the capacity from ~13% (<30 mAh g^{-1}) to ~68% (~154 mAh g^{-1}) of its initial value (Fig. S11d), accompanied by substantial recovery of the open-circuit voltage (inset, Fig. S11d). This photo-induced rejuvenation is attributed to strain relaxation and reactivation of Ti^{4+}/Ti^{3+} redox couples (Fig. 5), which collectively reopen blocked Li^+ diffusion pathways and release ions trapped in strain-pinned domains.

Together, these results demonstrate that the strain-engineered multiphase network provides a mechanically resilient scaffold for photo-assisted Li storage, combining fast ion transport, structural resilience, and light-activated defect chemistry. The system achieves a light-to-electrochemical con-

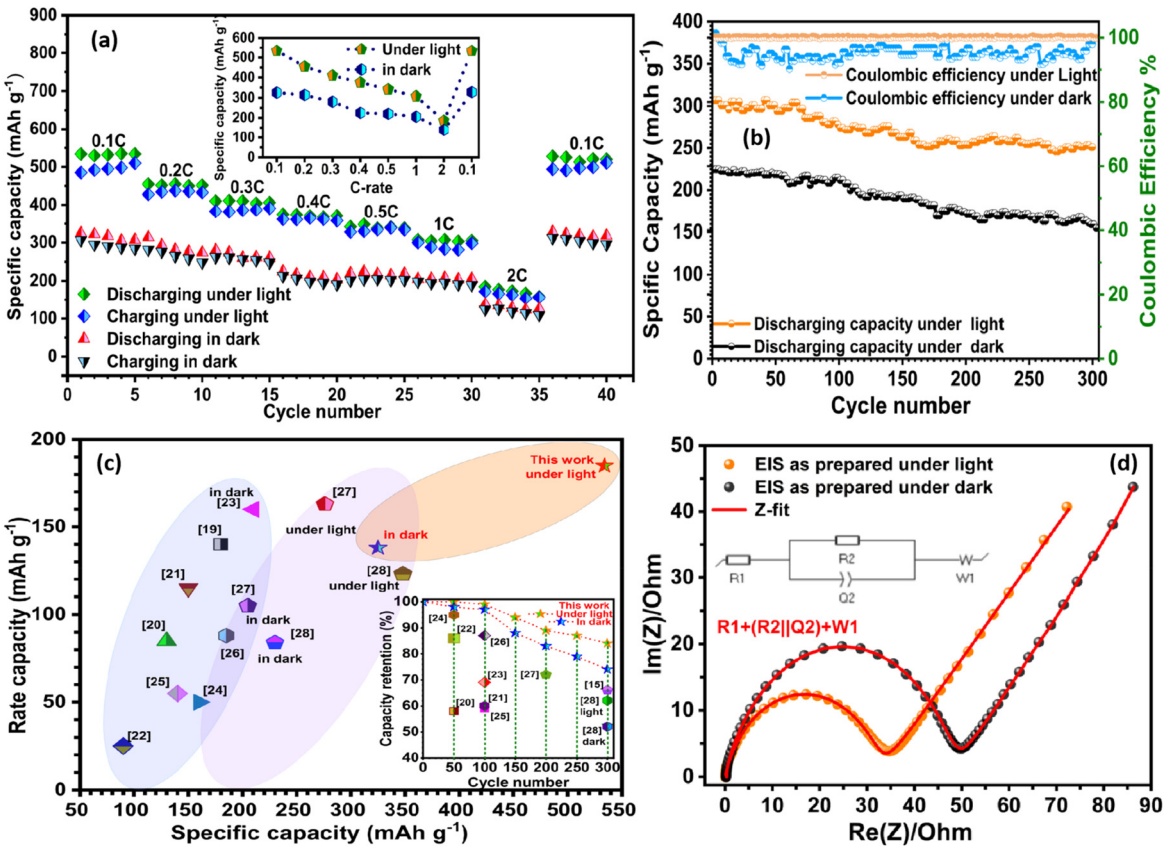

Fig. 4 Rate capability, long-term cycling, and mechanistic insights into photo-assisted charging and interfacial kinetics. (a) Rate performance from 0.1C to 2C under dark and illuminated conditions, showing enhanced capacities under illumination. (b) Cycling stability at 1C over 300 cycles: the illuminated electrode maintains ~280 mAh g^{-1} with nearly 100% coulombic efficiency. (c) Comparison of the $TiO_2/K_2Ti_4O_9$-rGO electrode with previously reported TiO_2 and titanate-based electrodes[20–29] under dark and illuminated conditions, demonstrating superior capacity and rate performance under illumination. Inset: comparison of capacity retention under illuminated and dark conditions, together with literature data for TiO_2-based electrodes, highlighting improved long-term stability under light-assisted operation. (d) Nyquist plots for fresh electrodes showing reduced R_{ct} under illumination; inset equivalent circuit model.

version efficiency of ~0.2% at a practical rate of 1C (*e.g.* see SI), highlighting its potential for high-performance photo-rechargeable lithium-ion batteries.

3.4. Mechanistic role of strain under illumination

The mechanistic role of interfacial strain is to mediate repeated volume changes during lithiation and delithiation without inducing lattice fatigue or interfacial failure. Fig. S10a illustrates the photo-assisted lithiation–delithiation mechanism of the $TiO_2/K_2Ti_4O_9$-rGO electrode. Under illumination, electron–hole pairs are generated within the TiO_2 polymorphs and the layered $K_2Ti_4O_9$ framework. Photogenerated electrons are efficiently extracted through the conductive rGO network toward the counter electrode, where they participate in Li^+ reduction. Simultaneously, valence-band holes facilitate Li^+ deintercalation from the active host, enabling continuous regeneration of redox-active Ti centres. This dual process allows the composite to act simultaneously as a Li-ion storage medium and as a photoactive absorber capable of converting incident light directly into stored electrochemical energy.[11,18]

Closely coupled interfaces between anatase, TiO_2(B), $K_2Ti_4O_9$, and rGO promote efficient charge separation and directional carrier transport while suppressing recombination. The multiphase architecture therefore supports enhanced capacity, accelerated kinetics, and improved cycling stability under illumination. Importantly, these benefits arise not only from photocarrier injection but also from strain-mediated stabilisation of the lattice during repeated electrochemical cycling.

Ex situ XPS collected after 300 charge–discharge cycles provides direct chemical evidence that interfacial strain engineering stabilises reversible redox activity while moderating fatigue-driven interfacial degradation (Fig. 5a, b and Fig. S13, S14). In the pristine electrode, Ti 2p spectra display characteristic Ti^{4+} doublets (Fig. S3). Upon discharge, both dark- and light-cycled electrodes exhibit shifts toward lower binding energies, corresponding to $Ti^{4+} \rightarrow Ti^{3+}$ reduction. Crucially, larger yet fully reversible shifts under illumination indicate deeper lithiation accommodated by strain-stabilised lattice deformation rather than irreversible structural collapse (Fig. 5a).

Upon charging, Ti 2p peaks return close to their pristine positions, confirming sustained Ti^{4+}/Ti^{3+} reversibility even after extended cycling.[29] In contrast to conventional TiO_2 electrodes, where fatigue-driven lattice damage often leads to irreversible Ti^{3+} accumulation, this behaviour demonstrates preservation of the active oxide framework. Li 1s signals appear only after cycling and exhibit lower binding energies under illumination, reflecting enhanced electronic coupling and reversible Li^+ storage enabled by strain-modulated interfaces

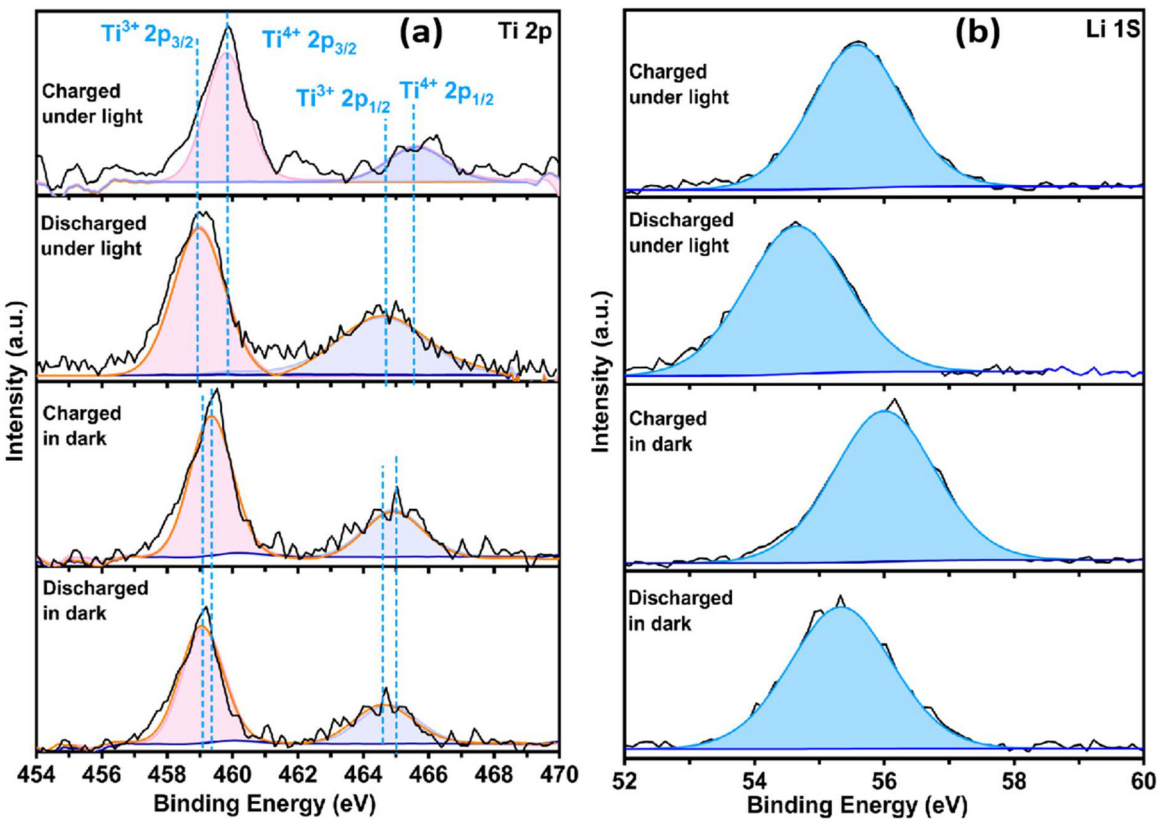

Fig. 5 Chemical stability and fatigue mitigation after prolonged cycling. XPS spectra of: (a) Ti 2p, showing reversible Ti^{4+}/Ti^{3+} redox behaviour after 300 cycles; and (b) Li 1s, confirming reversible lithium insertion and extraction.

(Fig. 5b). Based on these observations, the following reaction scheme is proposed.[29]

Lithiation (discharging). Photogenerated electrons promote Li^+ insertion into TiO_2 (anatase and TiO_2(B)) and $K_2Ti_4O_9$, forming Li_xTiO_2 and Li-intercalated/partially Li-substituted titanate ($Li_xK_2Ti_4O_9/K_{2-y}Li_yTi_4O_9$) while reducing Ti^{4+} to Ti^{3+}.

$$TiO_2/K_2Ti_4O_9\text{-rGO} + xLi^+ + xe^- \rightleftharpoons Li_x[TiO_2/K_2Ti_4O_9]\text{-rGO}.$$

Delithiation (photo-charging). Upon light removal or during electrochemical charge, Li^+ ions are extracted back into the electrolyte, and Ti^{3+} is re-oxidised to Ti^{4+}, restoring the oxide/titanate phases.

$$Li_x[TiO_2/K_2Ti_4O_9]\text{-rGO} \rightleftharpoons TiO_2/K_2Ti_4O_9\text{-rGO} + xLi^+ + xe^-.$$

This mechanistic picture highlights how interfacial strain, multiphase charge separation, and photocarrier injection cooperate to enable efficient light-assisted energy storage in the $TiO_2/K_2Ti_4O_9$-rGO electrode.

The superior photo-assisted performance arises from the interplay between built-in strain fields and photocarrier dynamics. Strain-modulated band alignment enhances electron–hole separation. $K_2Ti_4O_9$ layers provide low-energy Li^+ diffusion channels and stabilise TiO_2 (B). rGO rapidly extracts photogenerated electrons, suppressing recombination. Strain gradients reopen Li^+ pathways that become partially blocked during dark cycling.

Electrochemical impedance spectroscopy (EIS) (Fig. 4d and S12c) supports this mechanism. Illumination reduces the charge-transfer resistance (R_{ct}) in both fresh (from 55 to 33 Ω) and cycled electrodes, while steeper low-frequency slopes indicate enhanced Li^+ mobility. After 300 cycles, R_{ct} under illumination (~140 Ω) remains lower than in the dark (~165 Ω). This demonstrates sustained interfacial conductivity and light-mediated mitigation of resistance build-up.

Benchmarking against reported TiO_2-based electrodes[20–29] shows that the CHFS-derived multiphase composite outperforms noble-metal-modified, defect-engineered, and nanostructured TiO_2 systems (Fig. 4c and Table S4). Our multiphase composite electrode maintains higher retention over extended cycling, particularly under illumination (inset, Fig. 4c). These results underscore the effectiveness of the multiphase $TiO_2/K_2Ti_4O_9$-rGO architecture in mitigating degradation and improving long-term cycling stability through photo-assisted processes. This establishes interfacial strain engineering as an effective and scalable design strategy for high-performance light-responsive electrodes.

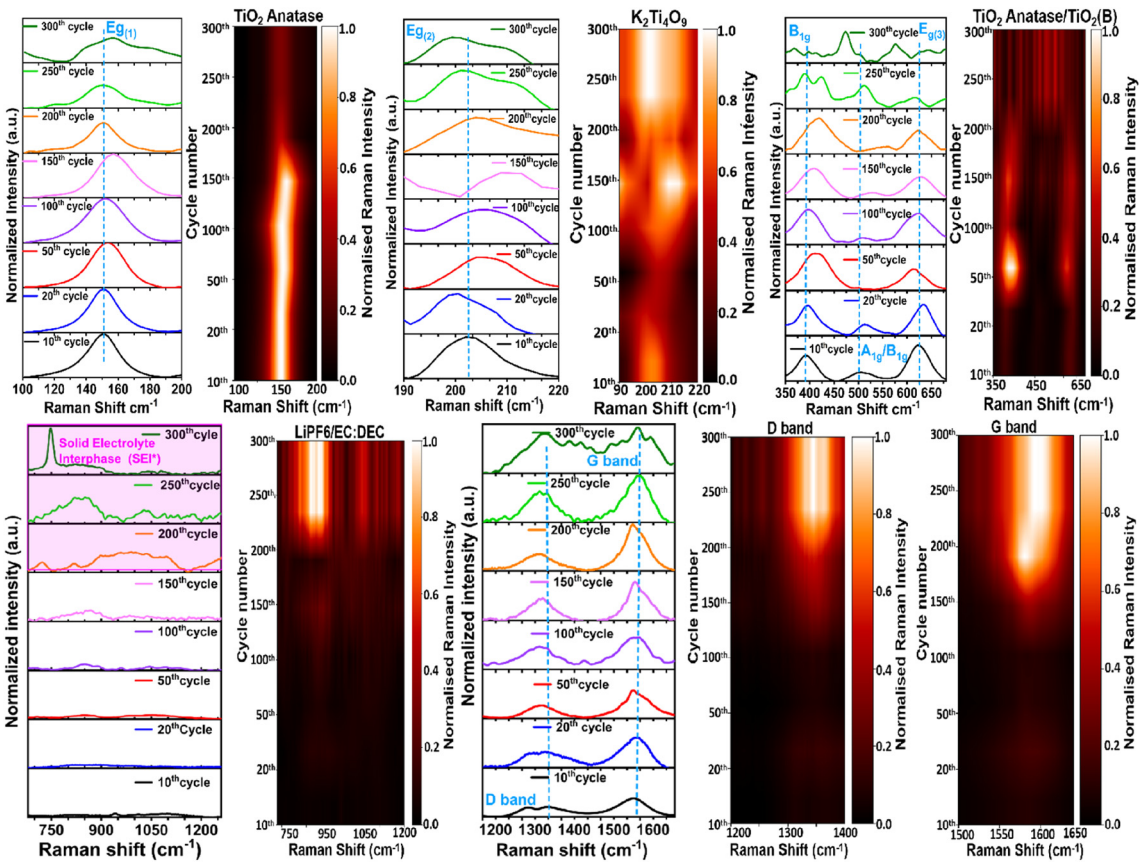

Fig. 6 Operando Raman tracking of structural evolution over 300 cycles. Time-resolved operando Raman spectra and heat maps showing stable Ti–O vibrational modes during early cycling (≤100), progressive broadening and red-shifting associated with microstrain and local disorder during intermediate cycling (150–200 cycles), and the emergence of SEI-related bands at 700–1100 cm^{-1} during later cycles (>200 cycles). These trends correlate with gradual capacity fading and identify interfacial SEI growth, rather than bulk phase collapse, as the dominant degradation mechanism.

3.5. Operando Raman microscopy: decoding the degradation mechanism

To assess the impact of strain engineering on long-term stability and delays to degradation, operando Raman spectroscopy was performed over 300 charge–discharge cycles (Fig. 6). Three distinct regimes can be identified.

Stage I: fatigue-resistant regime (<100 cycles). The characteristic vibrational modes of anatase, TiO_2(B), and $K_2Ti_4O_9$ remain sharp and unchanged, indicating fully reversible Li^+ intercalation with minimal structural perturbation. No disorder-related features are detected, demonstrating that the composite behaves as an elastically strain-accommodating lattice capable of hosting repeated ion insertion without damage accumulation. This regime correlates with the stable capacity retention observed during early galvanostatic cycling.

Stage II: fatigue onset (150–200 cycles). Gradual broadening and red-shifting of Ti–O vibrational modes in both anatase and TiO_2(B) are observed. This signifies a buildup of microstrain and local structural disorder. These spectroscopic signatures coincide with the onset of gradual capacity decay in the electrochemical data, reflecting cumulative lattice distortions that increasingly hinder uniform Li^+ transport.[30] Importantly, the underlying oxide phases remain intact, indicating that degradation is not associated with bulk phase instability.

Stage III: SEI-dominated fatigue-limited degradation (>200 cycles). A broad Raman feature emerging between 700–1100 cm^{-1} is observed. This is consistent with the growth of a thickened solid–electrolyte interphase (SEI), comprising LiF, Li_2CO_3, and $Li_xPO_yF_z$ species arising from $LiPF_6$ and carbonate decomposition.[31,32] Importantly, no Raman signatures indicative of TiO_2 or $K_2Ti_4O_9$ phase collapse are detected, confirming that the active oxide phases remain structurally intact. Degradation is therefore dominated by interfacial SEI accumulation. This is also confirmed by the confocal Raman imaging and XPS analysis of cycled electrodes (Fig. 5, 7, S13, S14 and S16).

Overall, the operando Raman analysis shows that the strain-engineered heterostructure maintains structural coherence for substantially longer than conventional TiO_2 electrodes. Together with the post-mortem analyses, these observations suggest that long-term capacity fade is governed largely by progressive interfacial SEI growth rather than rapid collapse of the active phases. Under illumination, the onset of interfacial disorder is further delayed, consistent with photocarrier-assisted strain relaxation and the enhanced cycling stability observed experimentally.

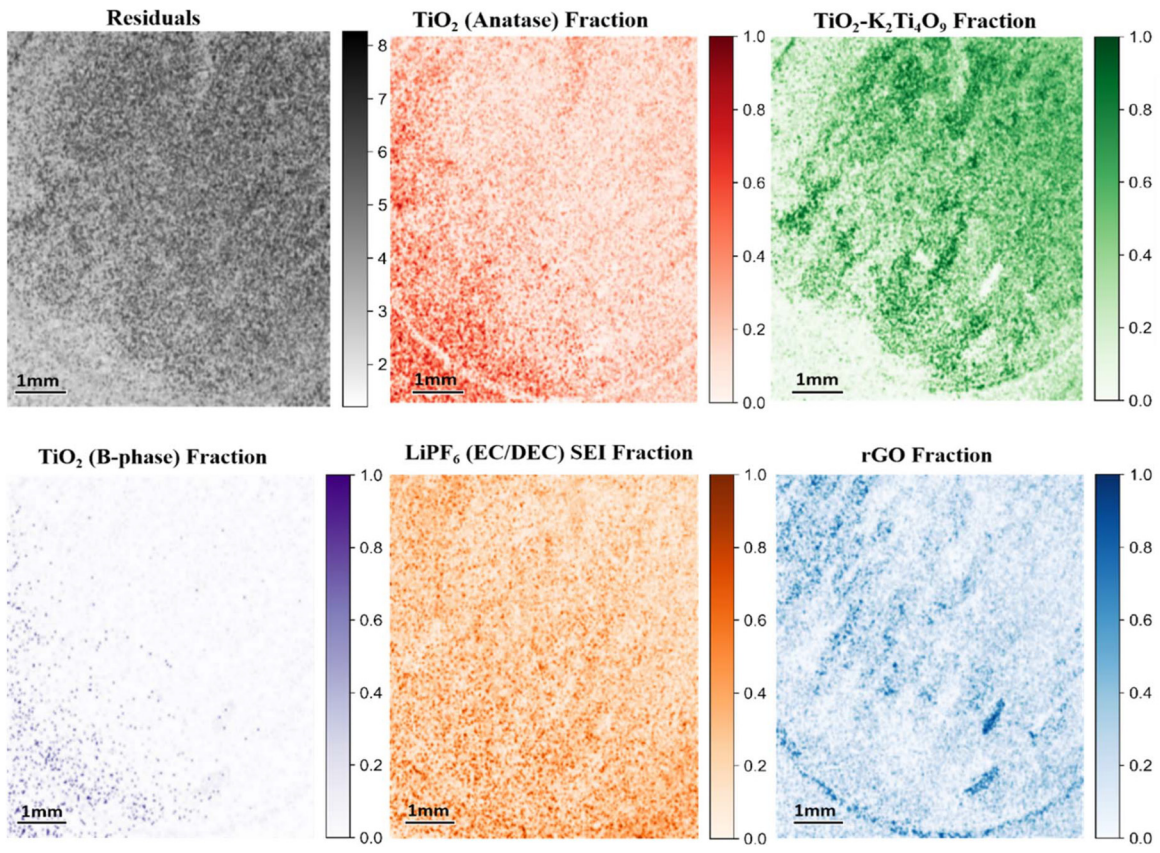

Fig. 7 Confocal Raman mapping of the $TiO_2/K_2Ti_4O_9$-rGO electrode after 300 cycles. NNLS-derived fraction maps reveal dominant $LiPF_6$-derived SEI coverage and attenuation of TiO_2, $K_2Ti_4O_9$, and rGO signals. The post-mortem Raman spectrum exhibits broad bands characteristic of fluorophosphate- and carbonate-based SEI species.

3.6. Cycled electrode analysis by confocal Raman imaging and NNLS

Confocal Raman mapping of the $TiO_2/K_2Ti_4O_9$rGO electrode after prolonged cycling reveals pronounced chemical and spatial evolution relative to the fresh electrode (Fig. 7 and S16). Due to substantial spectral overlap between TiO_2 polymorphs and $K_2Ti_4O_9$, non-negative least squares (NNLS) unmixing was applied to quantitatively separate the contributions of anatase TiO_2, TiO_2(B), $K_2Ti_4O_9$, and rGO. Whereas the pristine electrode exhibits well-defined NNLS fraction maps for each constituent phase, the cycled electrode is dominated by a $LiPF_6$-derived SEI component that spans nearly the entire mapped area.

The NNLS-derived SEI fraction map indicates extensive and relatively uniform surface coverage, consistent with post-mortem EDS detection of F- and P-containing species and confirming accumulation of $LiPF_6$-derived inorganic SEI products, including LiF, Li_2CO_3, and $Li_xPO_yF_z$. Direct spectroscopic evidence for SEI formation is provided by the post-mortem Raman spectrum of the electrode discharged after 300 cycles (Fig. S12b), which displays broad, merged features in the 400–900 cm^{-1} region characteristic of fluorophosphate- and carbonate-containing SEI species. The broad nature of these bands reflects the chemically mixed and partially amorphous character of the mature SEI.

As SEI coverage increases, the Raman fraction maps of anatase TiO_2 and $K_2Ti_4O_9$ exhibit reduced contrast and apparent dilution, indicating attenuation of their vibrational signatures by the overlying interfacial layer rather than intrinsic phase degradation. TiO_2(B), a comparatively weaker Raman scatterer, becomes particularly difficult to detect, consistent with preferential masking by the SEI. The rGO fraction map also shows reduced continuity and intensity, indicating that the conductive carbon network is increasingly buried beneath the SEI rather than structurally degraded. Increased residual intensity in the NNLS reconstruction further reflects the chemical complexity of the SEI, which cannot be fully represented by pristine reference spectra. Together, these observations demonstrate an SEI-dominated interface that limits Li^+ transport and suppresses photo-assisted electrochemical activity.

4. Conclusion

The central outcome of this work is the identification of interfacial strain as an important contributor to lattice-fatigue resistance and long-term electrode stability. By engineering intimately coupled oxide–oxide and oxide–carbon interfaces within a multiphase $TiO_2/K_2Ti_4O_9$-reduced graphene oxide architecture, we show that spatially distributed strain can help to accommodate reversible lattice breathing during repeated lithiation and delithiation, thereby mitigating crack formation, interfacial failure, and mechanically driven capacity fade. Using operando Raman microscopy, supported by *ex situ* and post-mortem characterisation, we find that strain relaxation is associated with delayed disorder accumulation and reduced interfacial degradation over extended cycling. Together, these results suggest that interfacial strain engineering is a promising strategy for improving the durability of high-capacity battery electrodes subject to large volume changes. More broadly, this approach may be relevant to lithium-, sodium-, and conversion-type chemistries, including lithium–sulfur systems, where mechanical degradation remains a major barrier to practical deployment.

Author contributions

M. T. S. and S. K. conceived the project and led conceptualization, methodology development, supervision, and project administration. M. T. S. secured funding for the project. M. T. S., S. K., and S. D. provided resources. M. N. performed investigation, data curation, and formal analysis, including all battery experiments and operando Raman microscopy measurements and mapping. K. N. contributed to investigation, data curation, and formal analysis. R. T. B. contributed and analysed TEM and XPS results. M. E. B. conducted confocal Raman imaging and NNLS analysis. R. K., S. B., and S. D. contributed to methodological development and formal data analysis. M. N. and M. T. S. wrote the original draft, and all authors reviewed and edited the manuscript.

Conflicts of interest

The authors declare no competing interests.

Data availability

The data supporting this publication can be accessed *via* DOI: 10.5281/zenodo.20072860. The Supplementary Information (SI) includes additional structural, spectroscopic, and electrochemical characterization data, including HR-TEM, XPS, UPS, UV–Vis, SEM/EDS, operando and confocal Raman analyses, lithium-ion diffusion calculations, strain estimation, light-to-electrochemical conversion efficiency calculations, post-mortem SEI analysis, NNLS Raman mapping, and comparative electrochemical performance data supporting the findings of this study. Supplementary Information is available at DOI: https://doi.org/10.1039/d6eb00089d.

Acknowledgements

We acknowledge financial support from the Photonics Place-based IAA and the EPSRC under the Photonics and Quantum Accelerator EPSRC grant (EP/Y024109/1). We also acknowledge financial support from EPSRC (UKRI647), Edinburgh Instruments Ltd, and London South Bank University. The authors acknowledge support from the British Council (grant numbers F41 and 2314). M. N. also thanks London South

Bank University for a PhD studentship. XPS and S/TEM measurements performed at the University of St Andrews, and we acknowledge support for the centre from the EPSRC (EP/L017008/1, EP/R023751/1 and EP/T019298/1).

References

1 J. Xu, J. Zhang, T. P. Pollard, Q. Li, S. Tan, S. Hou, H. Wan, F. Chen, H. He, E. Hu, K. Xu, X. Q. Yang, O. Borodin and C. Wang, *Nature*, 2023, **614**, 694–700.
2 C. Liu, F. Roters and D. Raabe, *Nat. Commun.*, 2024, **15**, 7970.
3 G.-L. Xu, X. Liu, X. Zhou, C. Zhao, I. Hwang, A. Daali, Z. Yang, Y. Ren, C.-J. Sun, Z. Chen, Y. Liu and K. Amine, *Nat. Commun.*, 2022, **13**(1), 436.
4 H. Zhang, J. Li, J. Liu, Y. Gao, Y. Fan, X. Liu, C. Guo, H. Liu, X. Chen, X. Wu, Y. Liu, Q. Gu, L. Li, J. Wang and S.-L. Chou, *Nat. Commun.*, 2025, **16**, 2520.
5 M. T. McDowell, S. W. Lee, W. D. Nix and Y. Cui, *Adv. Mater.*, 2013, **25**, 4966–4985.
6 K. Zhao, M. Pharr, L. Hartle, J. J. Vlassak and Z. Suo, *J. Power Sources*, 2012, **218**, 6–14.
7 Strategies towards enabling lithium metal in batteries:interphases and electrodes – Energy & Environmental Science (RSC Publishing) DOI: DOI: 10.1039/D1EE00767J, https://pubs.rsc.org/en/content/articlehtml/2021/ee/d1ee00767j, (accessed 11 January 2026).
8 P. Xiong, F. Zhang, X. Zhang, S. Wang, H. Liu, B. Sun, J. Zhang, Y. Sun, R. Ma, Y. Bando, C. Zhou, Z. Liu, T. Sasaki and G. Wang, *Nat. Commun.*, 2020, **11**, 3297.
9 Z. Dai, L. Liu and Z. Zhang, *Adv. Mater.*, 2019, **31**, 1805417.
10 K. Li, B. Li, J. Wu, F. Kang, J. K. Kim and T. Y. Zhang, *ACS Appl. Mater. Interfaces*, 2017, **9**, 35917–35926.
11 A. Lee, M. Vörös, W. M. Dose, J. Niklas, O. Poluektov, R. D. Schaller, H. Iddir, V. A. Maroni, E. Lee, B. Ingram, L. A. Curtiss and C. S. Johnson, *Nat. Commun.*, 2019, **10**, 4946.
12 R. Pandya, A. Mathieson, B. D. Boruah, H. B. de Aguiar and M. de Volder, *Nano Lett.*, 2023, **23**, 7288–7296.
13 A. Pujari, B. M. Kim, H. Abbasi, M. H. Lee, N. C. Greenham and M. De Volder, *ACS Energy Lett.*, 2024, **9**, 4024–4031.
14 Y. Chen, T. Wang, H. Tian, D. Su, Q. Zhang and G. Wang, *Adv. Mater.*, 2021, **33**, 2003666.
15 B. Mulligan-Clarke, C. Davids, M. Mushtaq, M. Leite, H. Geaney, S. Kellici and T. Kennedy, *J. Power Sources*, 2026, **668**, 239320.
16 S. Liang, X. Wang, R. Qi, Y. J. Cheng, Y. Xia, P. Müller-Buschbaum and X. Hu, *Adv. Funct. Mater.*, 2022, **32**, 2201675.
17 I. A. Baragau, J. Buckeridge, K. G. Nguyen, T. Heil, M. T. Sajjad, S. A. J. Thomson, A. Rennie, D. J. Morgan, N. P. Power, S. A. Nicolae, M. M. Titirici, S. Dunn and S. Kellici, *J. Mater. Chem. A*, 2023, **11**, 9791–9806.
18 K. Naoi, T. Kurita, M. Abe, T. Furuhashi, Y. Abe, K. Okazaki, J. Miyamoto, E. Iwama, S. Aoyagi, W. Naoi and P. Simon, *Adv. Mater.*, 2016, **28**, 6751–6757.
19 R. Khatoon, M. Nazir, R. T. Baker, M. Billing, S. Babar, S. Kellici, S. Dunn and M. T. Sajjad, *Adv. Funct. Mater.*, 2025, 2501498.
20 W. Song, Q. Jiang, X. Xie, A. Brookfield, E. J. L. McInnes, P. R. Shearing, D. J. L. Brett, F. Xie and D. J. Riley, *Energy Storage Mater.*, 2019, **22**, 441–449.
21 J. Ma, K. G. Reeves, A.-G. Porras Gutierrez, M. Body, C. Legein, K. Kakinuma, O. J. Borkiewicz, K. W. Chapman, H. Groult, M. Salanne and D. Dambournet, *Chem. Mater.*, 2017, **29**, 8313–8324.
22 Y. Cai, H. E. Wang, X. Zhao, F. Huang, C. Wang, Z. Deng, Y. Li, G. Cao and B. L. Su, *ACS Appl. Mater. Interfaces*, 2017, **9**, 10652–10663.
23 M. Zhang, K. Yin, Z. D. Hood, Z. Bi, C. A. Bridges, S. Dai, Y. S. Meng, M. P. Paranthaman and M. Chi, *J. Mater. Chem. A*, 2017, **5**, 20651–20657.
24 D. H. Lee, B. H. Lee, A. K. Sinha, J. H. Park, M. S. Kim, J. Park, H. Shin, K. S. Lee, Y. E. Sung and T. Hyeon, *J. Am. Chem. Soc.*, 2018, **140**, 16676–16684.
25 Y. Qiu, K. Yan, S. Yang, L. Jin, H. Deng and W. Li, *ACS Nano*, 2010, **4**, 6515–6526.
26 T. D. Deepa, S. Mohapatra, S. V. Nair, A. S. Nair and A. K. Rai, *Sustainable Energy Fuels*, 2017, **1**, 138–144.
27 D. Imazeki, C. C. Van Gils, K. Nishio, R. Shimizu and T. Hitosugi, *ACS Appl. Energy Mater.*, 2020, **3**, 8338–8343.
28 Z. Ma, S. Wang, Z. Ma, J. Li, L. Zhao, Z. Li, S. Wang, Y. Shuang, J. Wang, F. Wang, W. Xia, J. Jian, Y. He, J. Wang, P. Guo and H. Wang, *Nano-Micro Lett.*, 2025, **17**, 74.
29 W. Yan, J. Wang, Q. Hu, J. Fu, M. K. Albolkany, T. Zhang, X. Lu, F. Ye and B. Liu, *Nano Res.*, 2024, **17**, 2655–2662.
30 M. H. Kim, T. U. Wi, J. Seo, A. Choi, S. Ko, J. Kim, U. Jung, M. S. Kim, C. Park, S. Jin and H. W. Lee, *Nano Lett.*, 2023, **23**, 3582–3591.
31 R. Pandya, A. Mathieson, B. D. Boruah, H. B. de Aguiar and M. de Volder, *Nano Lett.*, 2023, **23**, 7288–7296.
32 Y. S. Hu and H. Pan, *ACS Energy Lett.*, 2022, **7**, 4501–4503.